

The interplay of geometry and coarsening in multicomponent lipid vesicles under the influence of hydrodynamics

Elena Bachini,¹ Veit Krause,¹ and Axel Voigt^{1,2,3}

¹*Institute of Scientific Computing, TU Dresden, Germany*

²*Center for Systems Biology Dresden, Germany*

³*Cluster of Excellence, Physics of Life, TU Dresden, Germany*

(Dated: 9 February 2023)

We consider the impact of surface hydrodynamics on the interplay between curvature and composition in coarsening processes on model systems for biomembranes. This includes scaling laws and equilibrium configurations, which are investigated by computational studies of a surface two-phase flow problem with additional phase-depending bending terms. These additional terms geometrically favor specific configurations. We find that as in 2D the effect of hydrodynamics strongly depends on the composition. In situations where the composition allows a realization of a geometrically favored configuration, the hydrodynamics enhances the evolution into this configuration. We restrict our model and numerics to stationary surfaces and validate the numerical approach with various benchmark problems and convergence studies.

I. INTRODUCTION

The interplay between curvature and composition is a ubiquitous structural feature for biomembranes and it plays a key role in biological functions and synthetic membrane-based applications (Ref. 1). Various simplified membrane models have been developed to mimic the heterogeneous organization of biomembranes in order to understand this complex interplay. Among them, there are multicomponent giant unilamellar vesicles (GUV), which feature liquid-ordered and disordered phases. The complexity of these synthetic systems is strongly reduced and they are ideally suited to study phase separation and coarsening of the lipid phases.

A comprehensive overview of such results is given in Ref. 2. In combination with theoretical models and simulations (Refs. 3 and 4) the different, sometimes contradicting, scaling results for the coarsening process could be clarified. Depending on the Saffmann-Delbrück number (Ref. 5), which is a hydrodynamic length relating the viscosity of the membrane and the surrounding bulk fluid $l_H = \eta_m/\eta_b$, the hydrodynamics is effectively 2D (3D) on spatial scales smaller than (greater than) l_H . Here, we consider the situation of $l_H \rightarrow \infty$ that allows to neglect the influence of the bulk fluid. Besides the influence of hydrodynamics, which is mainly studied on flat membranes (Refs. 3 and 4), composition plays an important role. Experimental and simulation studies have addressed the interplay between curvature and composition, see Refs. 6–14 for various approaches. However, a detailed investigation of the role of membrane curvature on spatial arrangements of lipid phases has only been considered recently using multicomponent scaffolded lipid vesicles (SLV) (Refs. 15–17). In these systems, non-spherical shapes are stabilized and the effect of spatially varying curvature on phase separation and coarsening can be considered. The results demonstrate the influence of curvature on the spatial arrangement of the lipid phases and the phase diagram. However, the focus of the modeling is on the equilibrium state and the influence of hydrodynamics is not considered in these approaches. Due to recent numerical developments in surface hydrodynamics (Refs. 18–23), here we combine these different investigations and study the influence

of membrane curvature on phase separation and coarsening under the influence of hydrodynamics.

We consider a mesoscale modeling approach building on Ref. 24, which provides an extension of the classical Canham/Helfrich model (Refs. 25 and 26) to two lipid phases, e.g., liquid-ordered and disordered phases. The corresponding energy reads:

$$\mathcal{F}_{JL} = \sum_{i=1}^2 \int_{\mathcal{S}_i} \kappa_i (\mathcal{H} - \mathcal{H}_{0,i})^2 + \bar{\kappa}_i \mathcal{H} \, d\mathcal{S} + \sigma \int_{\Gamma} ds, \quad (1)$$

with bending rigidity κ_i and Gaussian bending rigidity $\bar{\kappa}_i$, spontaneous curvatures $\mathcal{H}_{0,i}$, mean and Gaussian curvatures \mathcal{H} and \mathcal{K} , and interfacial line tension σ . Here, \mathcal{S}_i , $i = 1, 2$, denotes the surface area of the i -th lipid phase, for which $\mathcal{S}_1 \cup \mathcal{S}_2 = \mathcal{S}$ and $\mathcal{S}_1 \cap \mathcal{S}_2 = \Gamma$. We consider $\mathcal{S} \subset \mathbb{R}^3$ a closed regular surface without boundary. The model can be extended by considering Lagrange multipliers to ensure area conservation or local inextensibility of the two phases. As long as $\bar{\kappa}_1 = \bar{\kappa}_2$ and topological changes in a possible evolution of \mathcal{S} are prevented, the Gaussian curvature term in Eq. (1) only contributes a constant to the energy and will therefore be neglected in the following. Eq. (1) (with $\bar{\kappa}_i = 0$) can be cast in a phase-field approximation, obtaining:

$$\mathcal{F}_{PF} = \int_{\mathcal{S}} \kappa(\phi) (\mathcal{H} - \mathcal{H}_0(\phi))^2 \, d\mathcal{S} + \tilde{\sigma} \int_{\mathcal{S}} \frac{\varepsilon}{2} \|\nabla_{\mathcal{S}} \phi\|^2 + \frac{1}{\varepsilon} W(\phi) \, d\mathcal{S}, \quad (2)$$

with phase-field function $\phi \in [-1, 1]$, double-well potential $W(\phi) = \frac{1}{4}(\phi^2 - 1)^2$, interface thickness ε , rescaled interfacial line tension $\tilde{\sigma} = \sigma \frac{3}{2\sqrt{2}}$, and surface gradient $\nabla_{\mathcal{S}}$. The bending rigidity $\kappa(\phi)$ and spontaneous curvature $\mathcal{H}_0(\phi)$ are smoothly interpolated between the values of the two phases, such that:

$$f(\phi) = \begin{cases} f_1 & \text{if } \phi = 1 \\ \frac{f_1 + f_2}{2} + \frac{f_1 - f_2}{4} \phi(3 - \phi^2) & \text{if } -1 < \phi < 1, \\ f_2 & \text{if } \phi = -1 \end{cases} \quad (3)$$

for $f = \kappa, \mathcal{H}_0$. A connection between Eqs. (2) and (1) can be established by formal matched asymptotic or Γ -convergence if $\varepsilon \rightarrow 0$, following Ref. 10, 12, and 27. Possibilities to also consider the Gaussian curvature term and constraints on area and local inextensibility in the phase-field context have been discussed in Refs. 10, 28, and 29.

While the minimization of \mathcal{F}_{JL} and \mathcal{F}_{PF} with respect to \mathcal{S} and Γ , or \mathcal{S} and ϕ , respectively, has been discussed in the literature (see, e.g., Refs. 9, 10, 27, 29–31), here we consider the special case of a stationary surface \mathcal{S} . This reduces the problem to the evolution of Γ or ϕ on a given surface and is mathematically related to so-called geodesic evolution equations and their phase-field approximations. The conserved evolution of ϕ is a surface Cahn-Hilliard model with additional curvature terms:

$$\partial_t \phi = \nabla_{\mathcal{S}} \cdot (m \nabla_{\mathcal{S}} \mu), \quad (4)$$

$$\begin{aligned} \mu = & \kappa'(\phi)(\mathcal{H} - \mathcal{H}_0(\phi))^2 - 2\kappa(\phi)(\mathcal{H} - \mathcal{H}_0(\phi))\mathcal{H}_0'(\phi) \\ & + \tilde{\sigma} \left(-\varepsilon \Delta_{\mathcal{S}} \phi + \frac{1}{\varepsilon} W'(\phi) \right), \end{aligned} \quad (5)$$

with mobility m , chemical potential μ , surface divergence $\nabla_{\mathcal{S}} \cdot$, and Laplace-Beltrami operator $\Delta_{\mathcal{S}} = \nabla_{\mathcal{S}} \cdot \nabla_{\mathcal{S}}$. Eqs. (4) and (5) are defined on \mathcal{S} and need to be supplemented with appropriate initial conditions for ϕ . For $\varepsilon \rightarrow 0$ one obtains the corresponding surface Mullins-Sekerka type model (Ref. 12), for which equilibrium solutions have been analyzed in detail in Refs. 15 and 16. The corresponding experimental setting for the considered case of a stationary surface are the mentioned scaffolded lipid vesicles (SLV) with two lipid phases (Ref. 17). They provide an ideal test case to study curvature-induced effects in phase separation and coarsening of lipid domains and can be used for validation.

With recent developments in the modeling and simulation of surface fluids (Refs. 19–21, 32–38), it becomes feasible to also consider the surface viscosity of the liquid phases in such systems and study the evolution toward the equilibrium solutions. This leads to surface two-phase flow problems. The corresponding model to the Cahn-Hilliard like Eqs. (4) and (5) reads:

$$\partial_t \mathbf{u} + \nabla_{\mathbf{u}} \mathbf{u} = -\nabla_{\mathcal{S}} \tilde{p} + \frac{2}{\text{Re}} \text{div}_{\mathcal{S}} \boldsymbol{\sigma}(\mathbf{u}) + \mu \nabla_{\mathcal{S}} \phi, \quad (6)$$

$$\nabla_{\mathcal{S}} \cdot \mathbf{u} = 0, \quad (7)$$

$$\partial_t \phi + \nabla_{\mathbf{u}} \phi = \nabla_{\mathcal{S}} \cdot (m \nabla_{\mathcal{S}} \mu), \quad (8)$$

$$\begin{aligned} \mu = & \kappa'(\phi)(\mathcal{H} - \mathcal{H}_0(\phi))^2 \\ & - 2\kappa(\phi)(\mathcal{H} - \mathcal{H}_0(\phi))\mathcal{H}_0'(\phi) \\ & + \tilde{\sigma} \left(-\varepsilon \Delta_{\mathcal{S}} \phi + \frac{1}{\varepsilon} W'(\phi) \right), \end{aligned} \quad (9)$$

with tangential surface velocity \mathbf{u} , rescaled surface pressure \tilde{p} , surface stress tensor $\boldsymbol{\sigma}(\mathbf{u}) = \frac{1}{2}(\nabla_{\mathcal{S}} \mathbf{u} + \nabla_{\mathcal{S}}^T \mathbf{u})$, surface divergence for tensor fields $\text{div}_{\mathcal{S}}$, and surface Reynolds number Re . The convective terms are defined by $[\nabla_{\mathbf{u}} \mathbf{u}]_i = \nabla_{\mathcal{S}} u_i \cdot \mathbf{u}$, $i = 0, 1, 2$, and $\nabla_{\mathcal{S}} \phi \cdot \mathbf{u}$. Eqs. (6)–(9) are defined on \mathcal{S} and supplemented by initial conditions for ϕ and \mathbf{u} . We consider $\mathbf{u}(\mathbf{x}, t) = (u_1(\mathbf{x}, t), u_2(\mathbf{x}, t), 0)$ with components corresponding

to the local basis vectors $\mathbf{e}_1(\mathbf{x}), \mathbf{e}_2(\mathbf{x})$ and surface normal $\boldsymbol{\nu}(\mathbf{x})$. As we have the relation:

$$\begin{aligned} 2 \text{div}_{\mathcal{S}} \boldsymbol{\sigma}(\mathbf{u}) &= \text{div}_{\mathcal{S}} (\nabla_{\mathcal{S}} \mathbf{u}) + \text{div}_{\mathcal{S}} (\nabla_{\mathcal{S}}^T \mathbf{u}) \\ &= -\Delta_{\mathcal{S}}^{\text{DR}} \mathbf{u} + \mathcal{H} \mathbf{u} + \nabla_{\mathcal{S}} (\nabla_{\mathcal{S}} \cdot \mathbf{u}) + \mathcal{H} \mathbf{u} \\ &= -\Delta_{\mathcal{S}}^{\text{DR}} \mathbf{u} + 2\mathcal{H} \mathbf{u}, \end{aligned}$$

with Laplace-deRham operator $\Delta_{\mathcal{S}}^{\text{DR}}$, the surface Navier-Stokes part corresponds to previous formulations on stationary surfaces (Refs. 18, 32, 34, 35, 39–43).

The model is a surface Navier-Stokes-Cahn-Hilliard like equation, a generalization of the classical “Model H” (Refs. 44 and 45) to surfaces. For simplicity, we only consider the case of equal density and equal viscosity for the two phases. More general approaches emerge by considering the models compared in Ref. 46 and extend them to surfaces. We refer to Ref. 23 for an extension to surfaces of the thermodynamically consistent model proposed in Ref. 47. The combination of the asymptotic analysis in Ref. 12 for surface Cahn-Hilliard equations with matched asymptotic for Navier-Stokes-Cahn-Hilliard equations (Refs. 47–49) should allow to obtain the corresponding sharp interface surface two-phase flow problems. Previous numerical studies of Eqs. (6)–(9), such as Refs. 19, 22, and 23, are restricted to simply connected surfaces, special geometries or only consider lower order methods. None of the previous approaches takes into account the additional curvature terms emerging from the bending energy.

Here we propose a discretization based on surface finite elements (SFEM). We consider a higher-order surface approximation and solve Eqs. (6)–(9) using an operator splitting approach. The scalar-valued convected surface Cahn-Hilliard equation is solved by the scalar SFEM (Ref. 50) and for the surface Navier-Stokes equations the vector-valued SFEM (Ref. 51) is used. Discretization in time considers a semi-implicit finite difference approach. We validate each part and demonstrate convergence with potential optimal order.

The overall scheme is used to study curvature-induced effects in phase separation and coarsening. Considering a geometry with regions of two distinct mean curvatures and choosing κ_i or $\mathcal{H}_{0,i}$ correspondingly allows to determine the spatial arrangement of the lipid phases. Phase-dependent properties in the bending rigidity κ influence the coarsening process: the lipid phase with lower bending rigidity is guided toward regions of higher mean curvature, while the lipid phase with higher bending rigidity is guided toward regions of lower mean curvature. This behavior is known for the equilibrium configuration and has been demonstrated experimentally together with a geometric influence of the phase diagram (Ref. 17). The same effect can be achieved by specifying the spontaneous curvatures $\mathcal{H}_{0,i}$ to values that match the mean curvature of the different regions. Not only the phase diagram and equilibrium arrangements are influenced by the underlying geometry, but also the evolution toward this state changes. As in 2D and 3D, the coarsening process can be influenced by the flow and can lead to faster coarsening. However, the theoretical prediction for viscous hydrodynamic scaling of the interface length $l \sim t^{-1}$ could not be observed. Depending on the composition and the Reynolds number Re , we obtain $l \sim t^{-\alpha}$ with

$\frac{1}{3} \leq \alpha \leq \frac{2}{3}$, which is in agreement with theoretical and simulation results in 2D (Refs. 3 and 4) and simulations in Ref. 22. Moreover, it has been measured in various experiments on giant unilamellar vesicles (GUV), see Ref. 2 for a review. We also consider the topology and geometry of the phases. When islands are formed, they become more circular if flow is considered. This is one of the reasons for the slowdown of the coarsening process under flow for low compositions. Using the zeroth Betti number as a topological measure for connectivity of the phases (Refs. 52 and 53), and the interfacial shape distribution (ISD) as a geometrical measure of the isolated patches (Refs. 54 and 55), the scaling behavior can be quantified further. The additional curvature terms emerging from the bending energy not only have a global effect on the dynamics but also influence the flow field locally. We quantify this behavior by establishing a relation between surface mean curvature and velocity in phase-separated regions.

The paper is structured as follows. A detailed description of the numerical approach together with convergence studies for each subproblem is given in Section II, while a systematic investigation of the results on phase separation and coarsening is presented in Section III. In Section IV, we discuss the results, draw conclusions, and give an outlook on possible model extensions.

II. NUMERICAL APPROACH

In this section we describe the discrete setting, starting from the approximation of the surface, the discrete functional spaces and, finally, we present the discrete version of Eqs. (6)-(9). We discuss implementational aspects, and validate the numerical approach by considering benchmark problems for each subproblem.

A. Surface approximation

We assume that the smooth surface \mathcal{S} is approximated by a discrete k -th order approximation \mathcal{S}_h . If $k = 0$, \mathcal{S}_h^0 is formed by the union of non-intersecting flat triangles with vertices on \mathcal{S} . For $k \geq 1$, we consider the bijective map $\mathbf{X} : \mathcal{S}_h^0 \rightarrow \mathcal{S}$

and $I_h^k(\mathbf{X}) = \mathcal{S}_h^k$. We can write that $\mathcal{T}_h(\mathcal{S}) = \cup_{i=1}^{N_T} T_i = \mathcal{S}_h^k$. In the following, we use $k = 2$. Surface quantities, when needed, are computed from the approximate surface \mathcal{S}_h . In particular, this is done for the approximate value of the surface normal $\boldsymbol{\nu}_h$ and the mean curvature \mathcal{H}_h . A more detailed description of the construction of higher-order surface approximation can be found in Refs. 56 and 57. An adaptive mesh is used to refine elements along the interface described implicitly by $\phi(\mathbf{x}, t) = 0$.

B. Surface finite element functional spaces

We consider the surface finite element spaces defined by:

$$\begin{aligned} V_h(\mathcal{S}_h) &= \{v_h \in C^0(\mathcal{S}_h) \cap W_0^1 \mid v_h|_T \in \mathcal{P}_{k_v}(T)\}, \\ Q_h(\mathcal{S}_h) &= \{q_h \in L_0^2(\mathcal{S}_h) \mid q_h|_T \in \mathcal{P}_{k_q}(T)\}, \\ W_h(\mathcal{S}_h) &= \{\psi_h \in C^0(\mathcal{S}_h) \mid \psi_h|_T \in \mathcal{P}_{k_\psi}(T)\}, \end{aligned}$$

where k_v, k_q, k_ψ denote the polynomial orders. We extend the space V_h to $\mathbf{V}_h(\mathcal{S}_h) = (V_h)^3$, the space of (three-dimensional) vector functions. Classical $\mathcal{P}_2 - \mathcal{P}_1$ Taylor-Hood elements are used for the Navier-Stokes equations, with polynomial order 2 for the velocity \mathbf{u} and 1 for pressure \bar{p} . \mathcal{P}_2 is used for discretizing the phase-field function ϕ and the chemical potential μ .

C. Discrete formulation

We can now write the semi-discrete formulation of Eqs. (6)-(9). The surface Cahn-Hilliard like and surface Navier-Stokes like equations are solved separately in an operator splitting approach. At every time step $t^n \in [0, T]$, we first solve the surface Cahn-Hilliard like Eqs. (8) and (9) and then solve the surface Navier-Stokes like Eqs. (6) and (7). For the time discretization, we apply an implicit Euler scheme for both systems.

In the following, we denote by $(\cdot, \cdot)_{\mathcal{S}_h}$ the approximation by the quadrature rule of the L^2 -inner product on the approximated surface \mathcal{S}_h . Note that, the quadrature order has to be chosen high enough such that test and trial functions and area elements are well integrated.

Problem 1 (Semi-discrete surface Cahn-Hilliard like problem) Find $(\phi_h, \mu_h) \in W_h \times W_h$ such that:

$$\begin{aligned} (\partial_t \phi_h^n, \psi_h)_{\mathcal{S}_h} + (\nabla_{\mathbf{u}^{n-1}} \phi_h^n, \psi_h)_{\mathcal{S}_h} &= -m(\nabla_{\mathcal{S}} \mu_h^n, \nabla_{\mathcal{S}} \psi_h)_{\mathcal{S}_h}, \\ (\mu_h^n, \xi_h)_{\mathcal{S}_h} &= \left(\kappa'(\phi_h^{n-1}) (\mathcal{H}_h - \mathcal{H}_0(\phi_h^{n-1}))^2, \xi_h \right)_{\mathcal{S}_h} \\ &\quad - 2 \left(\kappa(\phi_h^{n-1}) \mathcal{H}_0'(\phi_h^{n-1}) (\mathcal{H}_h - \mathcal{H}_0(\phi_h^{n-1})), \xi_h \right)_{\mathcal{S}_h} \\ &\quad + \tilde{\sigma} \varepsilon (\nabla_{\mathcal{S}} \phi_h^n, \nabla_{\mathcal{S}} \xi_h)_{\mathcal{S}_h} + \frac{\tilde{\sigma}}{\varepsilon} (W'(\phi_h^n), \xi_h)_{\mathcal{S}_h}, \end{aligned}$$

for all $(\psi_h, \xi_h) \in W_h \times W_h$.

This is a classical SFEM approach (Ref. 50) for scalar-

valued surface PDEs. Note that, as standard for Cahn-

Hilliard equations, we linearize the derivative of the double-well potential by a Taylor expansion of order one, i.e., $W'(\phi_h^n) \approx W'(\phi_h^{n-1}) + W''(\phi_h^{n-1})(\phi_h^n - \phi_h^{n-1}) = -2(\phi_h^{n-1})^3 + (3(\phi_h^{n-1})^2 - 1)\phi_h^n$. Following Ref. 49, we consider $m = \gamma\epsilon^2$ with $\gamma > 0$.

For the surface Navier-Stokes like problem, we drop the requirement of \mathbf{u} being tangential and enforce this condition by a penalty approach. This allows to consider a global coordinate system, the one of the embedding space \mathbb{R}^3 , and apply the classical scalar SFEM approach (Ref. 50) to each component, see Ref. 51 for a general discussion and Refs. 20, 35, 58, and 59 for specific realizations. For this setting, we consider $\mathbf{u}(\mathbf{x}, t) = (u_1(\mathbf{x}, t), u_2(\mathbf{x}, t), u_3(\mathbf{x}, t))$ with components corresponding to the global basis vectors $\mathbf{e}_1, \mathbf{e}_2$ and \mathbf{e}_3 of \mathbb{R}^3 . Under the assumption that the added penalization enforces $\mathbf{u} \cdot \boldsymbol{\nu} = 0$, Eqs. (6) and (7) read:

$$\partial_t \mathbf{u} + \nabla_{\mathbf{u}} \mathbf{u} = -\nabla_{\mathcal{S}} \tilde{p} + \frac{2}{\text{Re}} \text{div}_{\mathbf{P}} \boldsymbol{\sigma}(\mathbf{u}) + \mu \nabla_{\mathcal{S}} \phi + \beta(h)(\mathbf{u} \cdot \boldsymbol{\nu})\boldsymbol{\nu}, \quad (10)$$

$$\nabla_{\mathbf{P}} \cdot \mathbf{u} = 0, \quad (11)$$

with $\boldsymbol{\sigma} = \frac{1}{2}(\nabla_{\mathbf{P}} \mathbf{u} + \nabla_{\mathbf{P}} \mathbf{u}^T)$ using the tangential gradient $\nabla_{\mathbf{P}} \mathbf{u} = \mathbf{P} \nabla \mathbf{u}^e \mathbf{P}$, where \mathbf{u}^e is an extension of \mathbf{u} constant in normal direction, $\mathbf{P} = \mathbf{I} - \boldsymbol{\nu} \otimes \boldsymbol{\nu}$ is the surface projection and ∇ is the gradient of the embedding space \mathbb{R}^3 . The tan-

gential divergence is defined as $\nabla_{\mathbf{P}} \cdot \mathbf{u} = \text{tr}[\mathbf{P} \nabla \mathbf{u}^e]$ and $\text{div}_{\mathbf{P}}$ denotes the corresponding tangential divergence for tensor fields. The term $\nabla_{\mathbf{P}} \mathbf{u}$ is a pure tangential tensor field and relates to the covariant operator by $\nabla_{\mathbf{P}} \mathbf{u} = \nabla_{\mathcal{S}}(\mathbf{P} \mathbf{u}) - (\mathbf{u} \cdot \boldsymbol{\nu})\mathcal{B}$, where \mathcal{B} is the shape operator with $B_{ij} = -\nabla_{\mathcal{S}}^i v_j$. Similarly, it holds $\text{div}_{\mathbf{P}} \mathbf{u} = \text{div}_{\mathcal{S}}(\mathbf{P} \mathbf{u}) - (\mathbf{u} \cdot \boldsymbol{\nu})\mathcal{H}$, see Ref. 60. The additional term in Eq. (10) considers a penalization of the normal component of \mathbf{u} , with $\beta(h)$ a parameter depending on the mesh size. Therefore, if \mathbf{u} is tangential, Eqs. (10) and (11) coincide with Eqs. (6) and (7). If tangentiality is only approximated, Eqs. (10) and (11) provide an approximation to Eqs. (6) and (7), which has been considered previously for surface approximations with $k = 0$ and shown to converge experimentally (Refs. 20, 53, and 61) with order 1 for the L^2 error in \mathbf{u} . More detailed results only exist for the surface Stokes problem (Refs. 60 and 62). These studies show optimal order of convergence of order 3 for the L^2 error in \mathbf{u} for surface approximations with $k = 2$, if the additional terms $(\mathbf{u} \cdot \boldsymbol{\nu})\mathcal{B}$ and $(\mathbf{u} \cdot \boldsymbol{\nu})\mathcal{H}$ are considered with $\boldsymbol{\nu}$ approximated by order 2 and $\boldsymbol{\nu}$ in the penalization term approximated by order 3 and $\beta(h) = \frac{\beta}{h^2}$. These results are analytically known only for the surface vector-Laplace problem (Refs. 59 and 63), but expected also for the surface Stokes problem (Refs. 62 and 64). However, if only the error in the tangential component of \mathbf{u} is considered, the additional requirement on the higher-order approximation in $\boldsymbol{\nu}$ can be dropped, see Ref. 65. With these results, we consider the following problem.

Problem 2 (Semi-discrete surface Navier-Stokes like problem) Find $(\mathbf{u}_h, p_h) \in \mathbf{V}_h \times Q_h$ such that:

$$\begin{aligned} (\partial_t \mathbf{u}_h^n, \mathbf{v}_h)_{\mathcal{S}_h} + (\nabla_{\mathbf{u}_h^{n-1}} \mathbf{u}_h^n, \mathbf{v}_h)_{\mathcal{S}_h} &= (p_h^n, \nabla_{\mathcal{S}} \cdot \mathbf{v}_h)_{\mathcal{S}_h} - \frac{2}{\text{Re}} ((\boldsymbol{\sigma}(\mathbf{u}_h^n), \nabla_{\mathcal{S}} \mathbf{v}_h)_{\mathcal{S}_h} \\ &\quad + (\mu_h^n \nabla_{\mathcal{S}} \phi_h^n, \mathbf{v}_h)_{\mathcal{S}_h} + \frac{\beta}{h^2} ((\mathbf{u}_h^n \cdot \boldsymbol{\nu}_h) \boldsymbol{\nu}_h, \mathbf{v}_h)_{\mathcal{S}_h}), \\ (\nabla \cdot \mathbf{u}_h^n, q_h)_{\mathcal{S}_h} &= 0, \end{aligned}$$

for all $(\mathbf{v}_h, q_h) \in \mathbf{V}_h \times Q_h$.

D. Implementational aspects

The above-described discretization is implemented within the finite element toolbox AMDiS (Refs. 66 and 67), using the Dune-CurvedGrid library (Ref. 57) to handle the approximation of the surfaces. This environment allows for a straightforward parallelization by using the PETSc library. We use a Richardson iteration method with full LU preconditioner and MUMPS as direct linear solver.

E. Validation of numerical approach

We first consider Problem 1 and Problem 2 separately, ignoring both the coupling terms and the additional curvature terms. This reduces the problems to the surface Cahn-Hilliard and the

surface Navier-Stokes equations, respectively.

1. Surface Cahn-Hilliard equation

Different benchmark problems have been proposed for the surface Cahn-Hilliard model on a sphere. In Ref. 68 a rotational symmetric solution of the surface Mullins-Sekerka problem is constructed. As this is the sharp interface limit of the surface Cahn-Hilliard equation (Ref. 12), it allows to study the convergence of solutions of Problem 1 in the interface thickness $\epsilon \rightarrow 0$. We only consider this qualitatively. A quantitative convergence study is beyond the scope of this paper. For theoretical results in this direction in 2D we refer to Ref. 69.

We consider the unit sphere $\mathcal{S} = S^2$ ($R = 1$) with an annular domain \mathcal{S}_1 for the phase $\phi = 1$ defined by two concentric circles with geodesic radii $R_{\max} = 0.8$ and $R_{\min} = 0.4$ as ini-

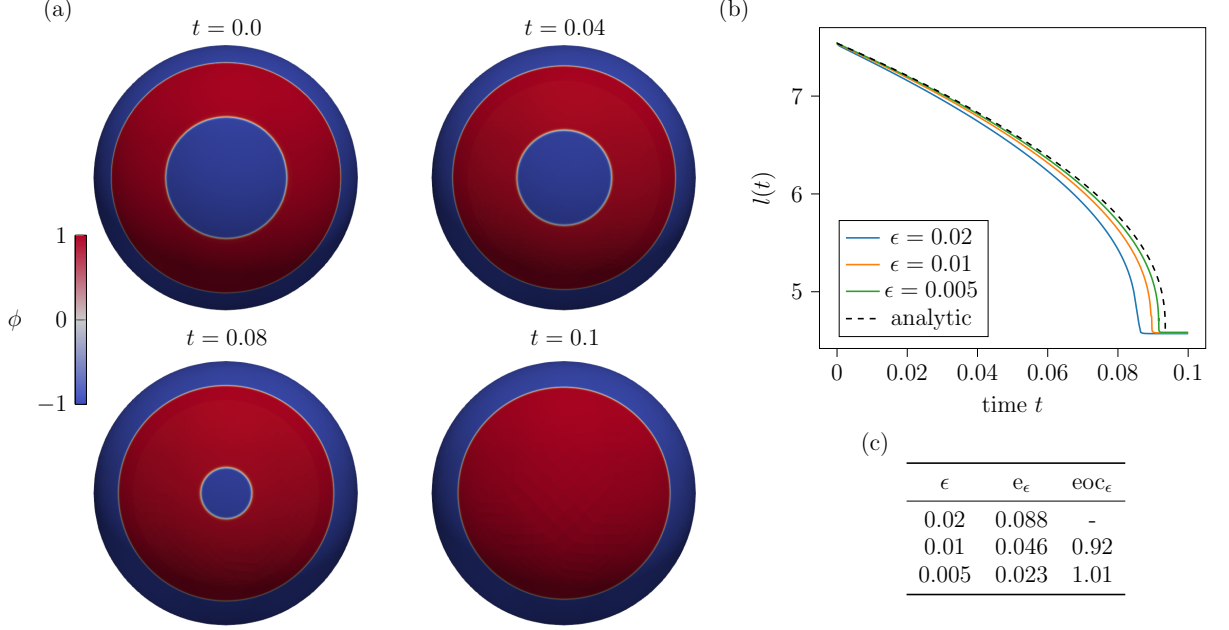


FIG. 1. Numerical solution for the surface Cahn-Hilliard model on benchmark problem (Ref. 68). (a) Numerical solution at times $t = 0.0, 0.04, 0.08, 0.1$ for $\epsilon = 0.005$. (b) Comparison between computed lengths in the cases of different values of ϵ and analytical solution. (c) Experimental order of convergence in the parameter ϵ , in the time interval $[0, 0.1]$. The error considers the difference in interface length over time.

tial condition (see Fig. 1-(a), top-left panel). In Eqs. (4) and (5), we set the parameters $m = 1$, $\tilde{\sigma} = \frac{3}{2\sqrt{2}}$ and $\kappa = \mathcal{H}_0 = 0$. We consider $\epsilon = 0.02, 0.01, 0.005$ to study the convergence in ϵ . As in our general setting, \mathcal{P}_2 elements are used for discretizing the phase-field function ϕ and the chemical potential μ . The mesh is adaptively refined to guarantee a resolution with at least 3 degrees of freedom around the interface, i.e., $\phi \in [-0.95, 0.95]$, and the time step τ is chosen as $\tau \sim h^2$.

Fig. 1-(a) shows the evolution at $t = 0.0, 0.04, 0.08, 0.1$ for $\epsilon = 0.005$. Both circular interfaces shrink until the smaller one collapses and a final configuration of a single geodesic circle for \mathcal{S}_1 is reached. Fig. 1-(b) shows the lengths of the interface computed as $l_\epsilon = \mathcal{F}_{PF}[\phi]$ for different ϵ and the analytic length l_* of the surface Mullins-Sekerka problem, see Ref. 68 for details. For each value of ϵ , we define the error:

$$e_\epsilon = \|l_\epsilon - l_*\|_{L^2(0,T)}, \quad (12)$$

where the integration in time is approximated by a trapezoidal rule over the time interval $[0, T]$, with $T = 0.1$. The experimental order of convergence is then defined by:

$$eoc_\epsilon = \log \left(\frac{e_{\epsilon, i-1}}{e_{\epsilon, i}} \right) / \log \left(\frac{\epsilon_{i-1}}{\epsilon_i} \right).$$

The results are reported in Fig. 1-(c) and indicate first-order convergence in ϵ .

More realistic situations of phase separation and coarsening on a sphere are considered in Ref. 70. We consider the proposed benchmark problem with a sphere of radius $R = 100$ and

initial condition defined by:

$$\phi(\theta, \varphi) = c_0 + \epsilon_{\mathcal{S}} [\cos(8\theta)\cos(15\varphi) + (\cos(12\theta)\cos(10\varphi))^2 + \cos(2.5\theta - 1.5\varphi)\cos(7\theta - 2\varphi)],$$

with $c_0 = 0.5$, $\epsilon_{\mathcal{S}} = 0.05$ and $\theta = \cos^{-1}(z/R)$ and $\varphi = \tan^{-1}(y/x)$ the polar and azimuth angles in a spherical coordinate system. Fig. 2-(a), top-left panel, shows the initial solution. In Eqs. (4) and (5) we set $m = 5$, $\tilde{\sigma} = \frac{3}{2\sqrt{2}}$ and $\kappa = \mathcal{H}_0 = 0$. We further consider a modified double-well potential $W(\phi) = \frac{2}{5}(\phi^2 - 1)^2$ and $\epsilon = 2$ to obtain the same model and parameter setting as in Ref. 70. Fig. 2-(a) shows the evolution at $t = 0, 200, 2000, 3.7e + 5$, and Fig. 2-(b) shows the scaling of the interface length l over time, on a mesh with $h = 0.41$ at the interface. Note that, for this benchmark problem, we consider a first-order surface approximation and \mathcal{P}_1 elements for the phase-field function ϕ and the chemical potential μ . As already demonstrated numerically in Refs. 71 and 72, the coarsening process is purely driven by line tension and the spherical geometry has no effect on the scaling behavior. As theoretically predicted for 2D, we obtain $l \sim t^{-1/3}$.

With analogous definitions as in the previous benchmark problem, we compute the error over different mesh refinements for a fixed $\epsilon = 2$, and the corresponding experimental order of convergence. We start from the same initial condition (see Fig. 2-(a), top-left panel) and then consider subsequent refinements of the region $\phi \in [-0.95, 0.95]$, with mesh sizes at the interface of $h = 1.26, 0.89, 0.63, 0.41, 0.31, 0.22$ and $h_* = 0.11$, which we set as reference level. We consider a final time $T = 200$ and choose a fixed time step $\tau = 1$ for all simulations.

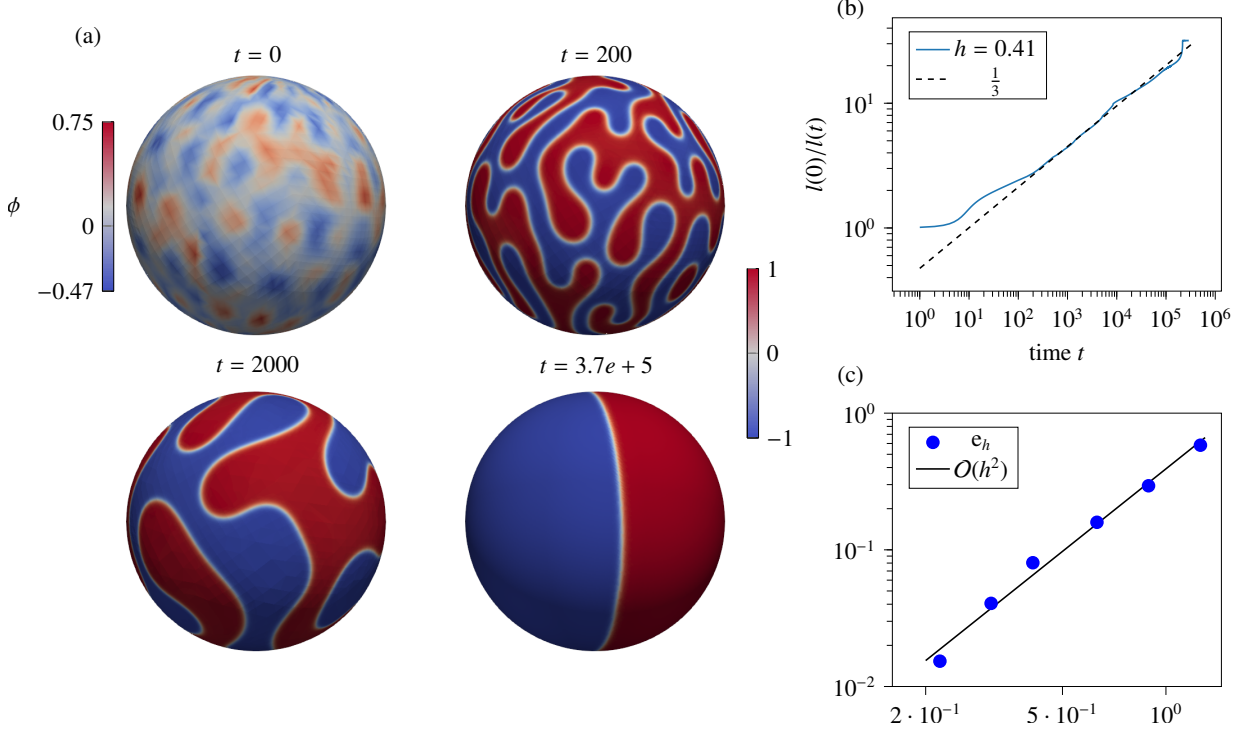


FIG. 2. Numerical solution for the surface Cahn-Hilliard model on benchmark problem (Ref. 70). (a) Approximate solution at times $t = 0, 200, 2000, t = 3.7e + 5$. (b) Inverse of the approximate interface length over time (normalized with the initial length), and interpolated line of order $1/3$. (c) Experimental order of convergence over refinement in the mesh parameter h in the time interval $[0, 200]$.

The numerical solutions look qualitatively equivalent to the one presented in Fig. 2-(a). Fig. 2-(c) shows the error values and indicate second-order convergence in h .

2. Surface Navier-Stokes equation

Different numerical methods have been proposed to solve the incompressible surface Navier-Stokes equations on stationary surfaces. One of the possibilities is to consider the vorticity/stream function formulation, where the problem is first transformed to a system of surface scalar-valued PDEs and then solved with established approaches such as surface FEM (Refs. 19, 32, and 34), trace FEM (Ref. 60), and spectral methods (Ref. 73). Formulations in \mathbf{u}, p variables have to deal with tangential vector fields and have been considered using discrete exterior calculus (DEC) (Ref. 33), surface FEM (Refs. 20, 21, 37, and 74), and trace FEM (Refs. 23 and 60). Also Lattice-Boltzmann approaches have been developed to solve the surface Navier-Stokes equations (Ref. 22). A precise benchmark problem has not yet been proposed. Here, we consider a setting that has been used to compare different numerical methods, see Ref. 33, and which takes into account geometric and topological implications. The surface \mathcal{S} is given by the level-set function $\phi(\mathbf{x}) = (a^2 + x_1^2 + x_2^2 + x_3^2)^2 - 4a^2(x_1^2 + x_2^2) - c^4$, with $\mathbf{x} = (x_1, x_2, x_3) \in \mathbb{R}^3$ and $a = 0.72$ and $c = 0.75^{75}$. The initial velocity is defined by $\mathbf{u}_0 = \boldsymbol{\nu} \times (0, 1, 1)$, and it is shown in Fig. 3-(a). We con-

sider the relaxation toward a Killing field and compute the kinetic energy $E = \frac{1}{2} \int_{\mathcal{S}} \|\mathbf{u}\|^2 d\mathcal{S}$. This energy dissipates and is bounded from below by the energy of the resulting Killing field. For $\text{Re} = 10$, the evolution is shown by streamlines in Fig. 3-(d). The final solution has two vortices located on the symmetry axis. Besides this qualitative agreement with Ref. 33, we analyze the incompressibility error $e_{\text{div} \mathbf{P}} = \|\text{div} \mathbf{P} \mathbf{u}\|_{L^\infty(L^2)}$ and the energy error $e_E = \|E - E_{\text{ref}}\|_{L^\infty}$ with respect to h and τ , where $\tau \sim h^2$. We take the DEC solution of Ref. 33 as a reference E_{ref} for $\text{Re} = 10$. Fig. 3-(b) indicates second-order convergence for the incompressibility error $e_{\text{div} \mathbf{P}}$, which corresponds to the result in Ref. 60 for the surface Stokes model and is assumed to be optimal. Fig. 3-(c) also indicates second-order convergence for the energy error e_E . The evolution of the kinetic energy E is shown in Fig. 3-(e) for different refinement levels, together with the reference solution taken from Ref. 33.

3. Coupling

For the coupling, we rely on established approaches in 2D for Navier-Stokes-Cahn-Hilliard equations. They are well tested on benchmark problems (Ref. 46) and can be one-to-one extended to surfaces. We therefore simply iterate Problem 1 and Problem 2 once for each time step. The additional curvature terms are of lower order and should not influence the numerical properties of the algorithm.

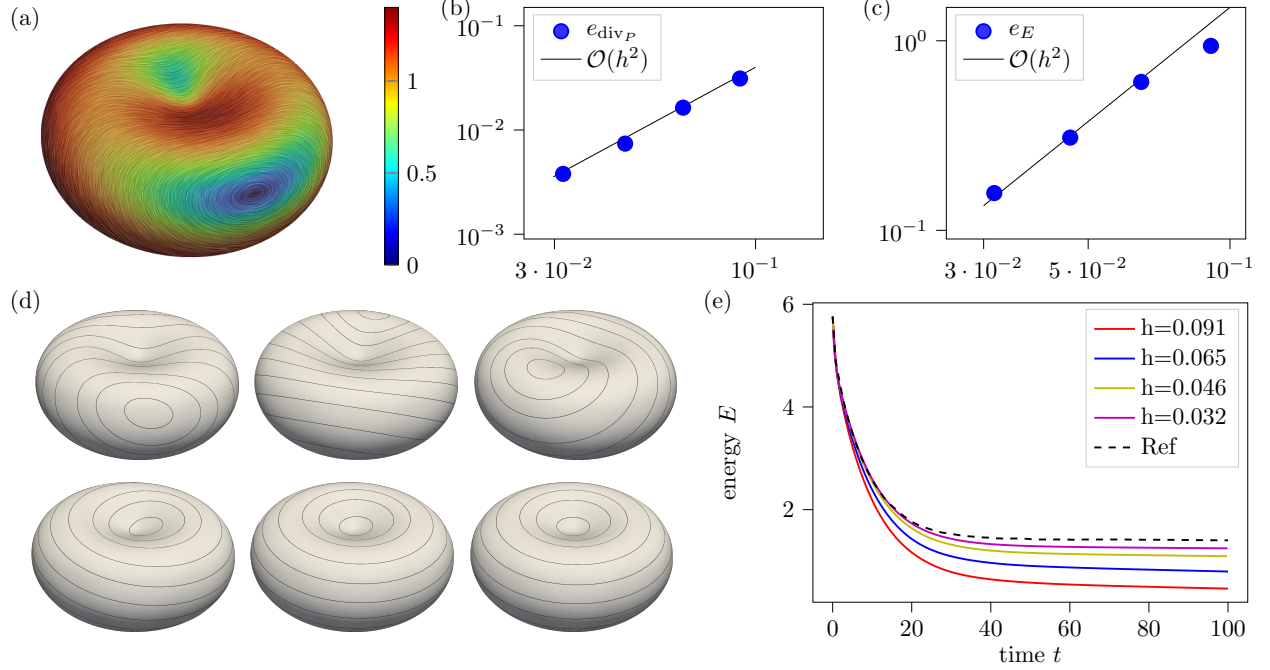


FIG. 3. Numerical solution for the surface Navier-Stokes equation. (a) Initial value of the velocity highlighted by a LIC-filter color code by the magnitude of the velocity. (b) Convergence study of the incompressibility error e_{div_P} . (c) Convergence study of the energy error e_E , with the corresponding DEC solution in Ref. 33 as reference. (d) Relaxation of the velocity field shown as snapshots of the streamlines for $t = 0, 10, 20, 50, 75, 100$ with the final Killing field. (e) Evolution of the kinetic energy E for different refinement levels together with the reference solution.

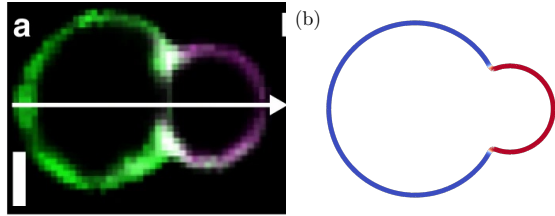


FIG. 4. Equilibrium configuration. Images of the equatorial plane for the phase-separated state. (a) Fluorescence intensity along the symmetry axis of a scaffolded lipid vesicle (SLV). The image is taken with permission from Ref. 17, Fig. 3. (b) Our simulation result for the final phase separated state on the same equatorial plane.

III. RESULTS

We consider a set of numerical experiments designed to investigate the influence of flow and of the additional curvature terms emerging from the bending contribution on coarsening in two-phase lipid membranes. We consider a geometry similar to the asymmetric dumbbell-shape (“snowman-shape”) in Ref. 17. It is formed by the union of two spheres with different radii: a sphere of radius $R_1 = 1$ intersects a sphere of radius $R_2 = 0.5$ with a smoothed intersection. Fig. 4 shows a section along the symmetry axis and the qualitative comparison with an

experimental result on a scaffolded lipid vesicle (SLV) taken from Ref. 17..

The considered geometry is ideally suited to explore the influence of the additional curvature terms. This influence has already been considered in Ref. 17 for equilibrium configurations and effects of the geometry on the phase diagram. Therefore, here we only focus on the dynamics. We consider $\kappa(\phi)$ as defined in Eq. (3), with $\kappa_1 = 0.001$ $\kappa_2 = 0.1$ and specify $\mathcal{H}_0(\phi) = \mathcal{H}_0 = 0$. We vary the Reynolds number, $\text{Re} = 3, 1$ and 0.1 , and we consider three sets of initial configurations. In particular, we set uniform distributed circles for the phase $\phi = 1$, and $\phi = -1$ elsewhere, such that the mean value is $0.5, 0.35$ and 0.16 , in order to represent a composition of $50 : 50, 65 : 35$ and $84 : 16$, respectively. The latter corresponds to the case where the phase $\phi = -1$ occupies the large sphere and the phase $\phi = 1$ the small sphere, as considered in the qualitative comparison with the experimental data (Fig. 4) and in the illustration of the coarsening process and surface flow (Fig. 5). In addition, we consider for comparison the evolution without flow, by solving Problem 1 with $\mathbf{u}^{n-1} = 0$. The results are marked as CH. Fig. 5 shows snapshots of the evolution of the phase-field function ϕ and the velocity \mathbf{u} for $\text{Re} = 1$ and composition $84 : 16$, as an example. We obtain a classical coarsening process, with the merging and coarsening of islands. However, due to the additional curvature terms resulting from the bending terms and the phase-specific bending rigidity κ ,

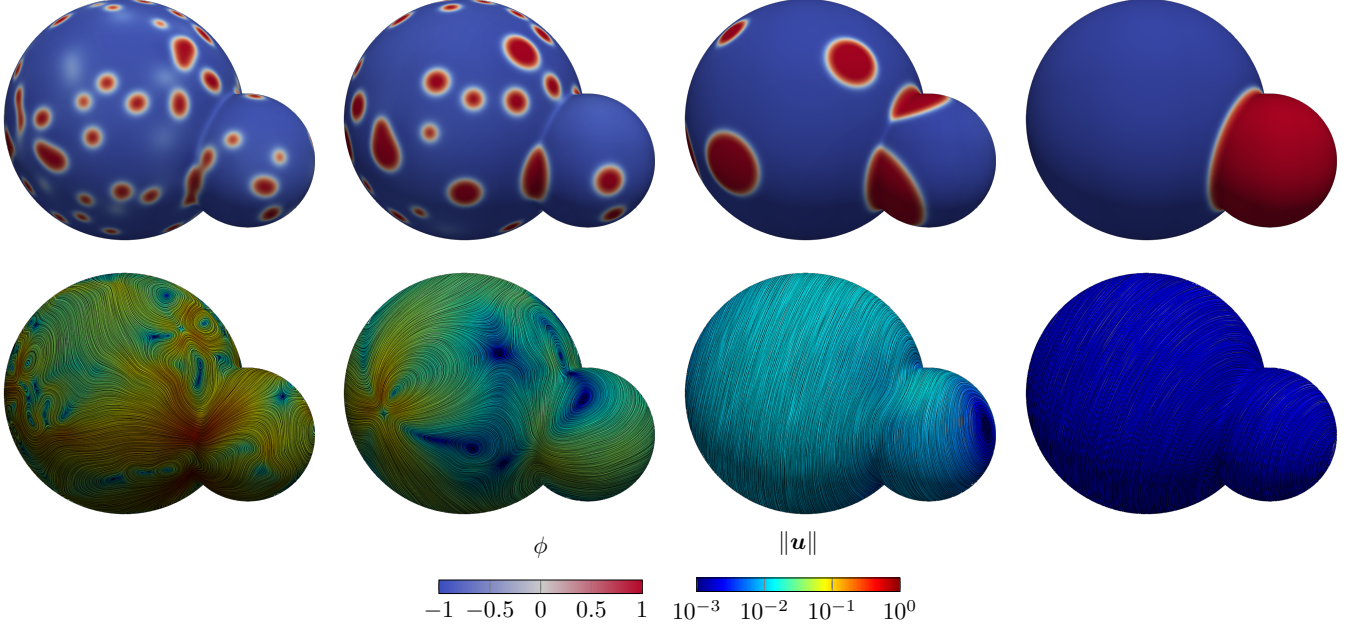


FIG. 5. Snapshots of the evolution of the two-phase flow problem at time instances $t = 0.2, 1.0, 10, 1200$ (from left to right). Top row: phase-field function ϕ . Bottom row: velocity \mathbf{u} , visualized by a LIC filter and color-coding according to the magnitude of the velocity in logarithmic scale.

the process is guided toward a final configuration with the phase $\phi = -1$ occupying the large sphere and the phase $\phi = 1$ occupying the small sphere. The surface flow is influenced by the geometry, but primarily by changes of the lipid patches with large magnitudes associated with merging events. At late times, the velocity is almost zero.

We first address the scaling behavior of the interface length. In Fig. 6, panels (a)-(c) show the results for the considered compositions and Reynolds numbers Re , together with the theoretically proposed scaling exponents for 2D: -1 for viscous hydrodynamic scaling, $-1/2$ for inertial hydrodynamic scaling, and $-1/3$ for diffusive scaling. We never observe fast coarsening associated with viscous hydrodynamic scaling. Only for a composition of 50 : 50 we observe a dependency of the scaling exponent on Re , at least within some time period. In Ref. 76, authors argue that self-similar growth is absent under the influence of flow and the scaling exponent results from an interplay of fast viscous hydrodynamic scaling and slow diffusive scaling, leading to values between $-2/3$ and $-1/3$ depending on Re . Our results on the dependency of the exponent on Re confirm this finding for the considered surface. However, our results also show a stagnation of the coarsening over a long time period. The solutions settle in local minima. We will analyze below that these local minima are induced by geometric properties of the surface. Only for some instances the solutions escape from these configurations and further coarsen to the equilibrium states. For the other compositions, i.e. 65 : 35 and 84 : 16, the flow field has only a minor effect and is no longer able to speed up the coarsening process. We obtain $l \sim t^{-1/3}$ up to late times for all considered Re . This is in agreement with the results obtained in Ref. 22 on a torus.

Their motivation for the effect is related to a faster relaxation to a circular shape for isolated patches under the influence of flow and, further, diffusive scaling for circular patches. In order to confirm this result, we analyze the connectivity of the phases and the interfacial shapes of the isolated patches. This can be done by computing topological and geometrical measures. The first measure we consider is defined by the zeroth Betti number N_{betti} , which counts isolated patches of the phase $\phi = 1$, see Refs. 52 and 53 for a similar characterization. This quantity is computed for each time instance and shown in Fig. 6, panels (d)-(f). The Betti number only weakly depends on Re , but we clearly see a dependency on the composition. While for the composition 50 : 50 the value is low at early times and further decays over time, for 65 : 35 we observe significantly larger Betti numbers but also a stronger decay in time. The large Betti numbers result from the formation of isolated patches and the strong decay can be associated with frequent merging events at the early stage of the coarsening process. The behavior for the composition 84 : 16 is similar to the case 65 : 35, with even larger Betti numbers at early times and even stronger decay. In this setting, patches are smaller and more isolated leading to fewer merging events, and the Betti number is mainly reduced by diffusive processes. Similar qualitative results on the number of patches have been considered on spherical unilamellar vesicles (Ref. 77). The interfacial shape of the isolated patches is measured by computing the interfacial shape distribution (ISD). The ISD is a probability density function for the probability of finding a point on the interface with specific principal curvatures. ISD is an established method to geometrically characterize interfacial morphology in materials science and fluid mechanics (Refs. 54, 55, 78, and 79). Adapted to our context

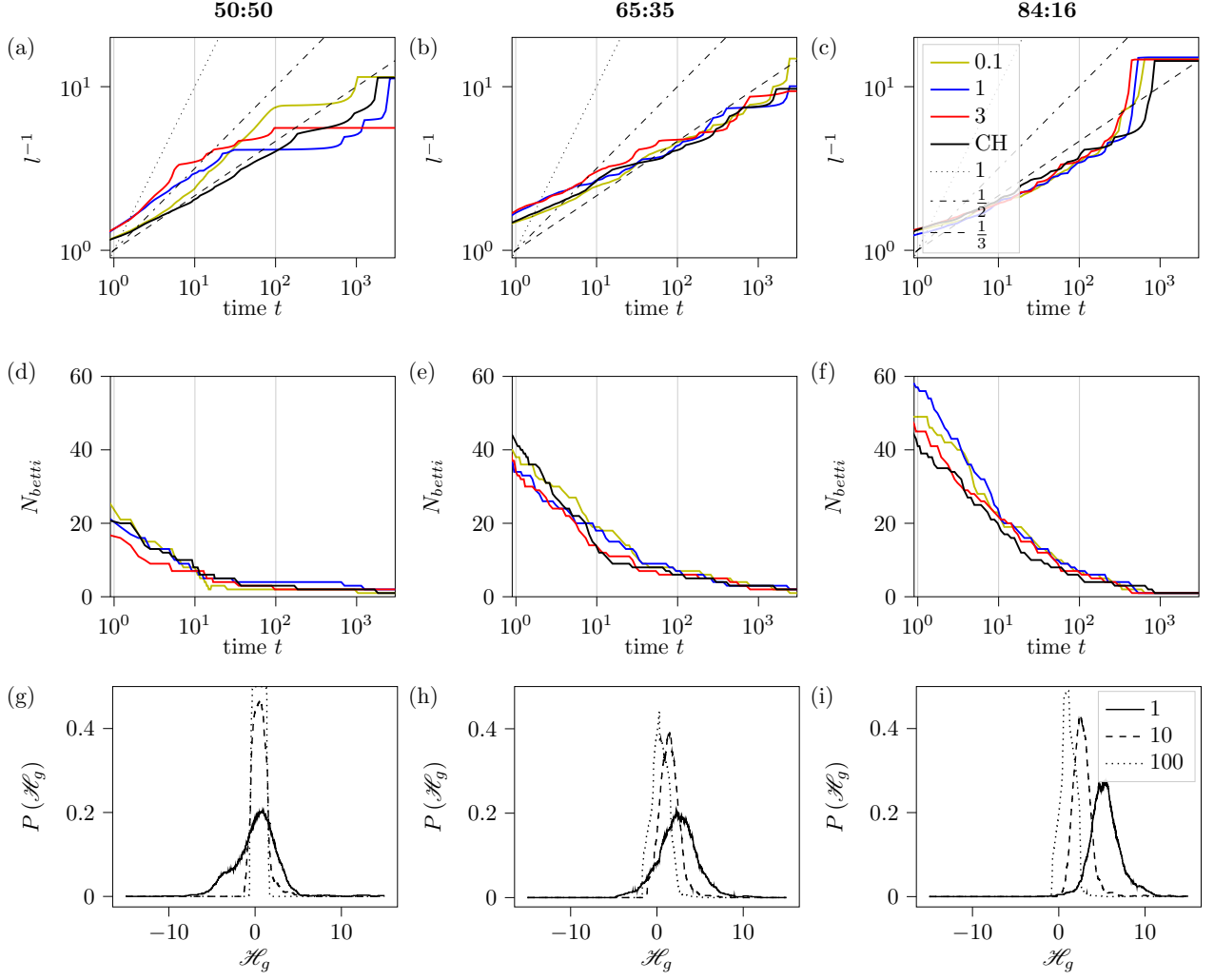


FIG. 6. Scaling of interface length, topological properties, and geometric features for different compositions and Reynolds numbers Re . (a)-(c) Scaling of the interface length together with theoretically predicted exponents in 2D. The legend corresponds to all panels and indicates the values for Re . (d)-(f) Evolution of zeroth Betti number. (g)-(i) Interfacial shape distribution (ISD) for the geodesic curvature \mathcal{H}_g at different time instances $t = 1, 10, 100$ for $Re = 1$. The corresponding time instances are highlighted in panels (a)-(f).

of an interface between two phases on a surface, the method considers the geodesic curvature \mathcal{H}_g and the corresponding probability density $P(\mathcal{H}_g)$.

We use a phase-field approximation to compute \mathcal{H}_g . In 2D the mean curvature \mathcal{H} can be approximated by the chemical potential, the variational derivative of the Cahn-Hilliard energy $\mathcal{F}_{CH} = \int_{\Omega} \frac{\epsilon}{2} \|\nabla \phi\|^2 + \frac{1}{\epsilon} W(\phi) d\Omega$, compare the matched asymptotic analysis of a classical Allen-Cahn equation (Ref. 80). In our case the chemical potential μ , as considered in Eq. (5) (with $\kappa = \mathcal{H}_0 = 0$ and $\tilde{\sigma} = \frac{2\sqrt{2}}{3}$), provides a diffuse interface approximation of the geodesic curvature \mathcal{H}_g , see Ref. 81 for the corresponding matched asymptotic analysis. The chemical potential μ can be computed from the phase-field function ϕ considering a weak formulation. Therefore,

we approximate \mathcal{H}_g by the convolution:

$$\mathcal{H}_g(\mathbf{y}) = \int_{\mathcal{S}} \frac{\epsilon}{2} (\nabla_{\mathcal{S}} \phi(\mathbf{x}), \nabla_{\mathcal{S}} \psi(\mathbf{x}, \mathbf{y})) + \frac{1}{\epsilon} W(\phi(\mathbf{x})) \psi(\mathbf{x}, \mathbf{y}), d\mathcal{S}$$

where $\psi(\mathbf{x}, \mathbf{y})$ is a mollifier and $\mathbf{x} \in \mathcal{S}$ and $\mathbf{y} \in \{\phi = 0\}$. We consider $Re = 1$ and compare $P(\mathcal{H}_g)$ at times $t = 1, 10, 100$, see Fig. 6, panels (g)-(i). For all compositions, the ISD sharpens over time and the mean value evolves to small positive values, indicating an evolution toward large circular shapes. However, we also see differences with respect to the different compositions. For the composition of 50 : 50, the ISD has a significant portion for negative \mathcal{H}_g at early times, and therefore concave parts, which indicates a more bicontinuous-like structure. In contrast, the ISD at early times for the composition

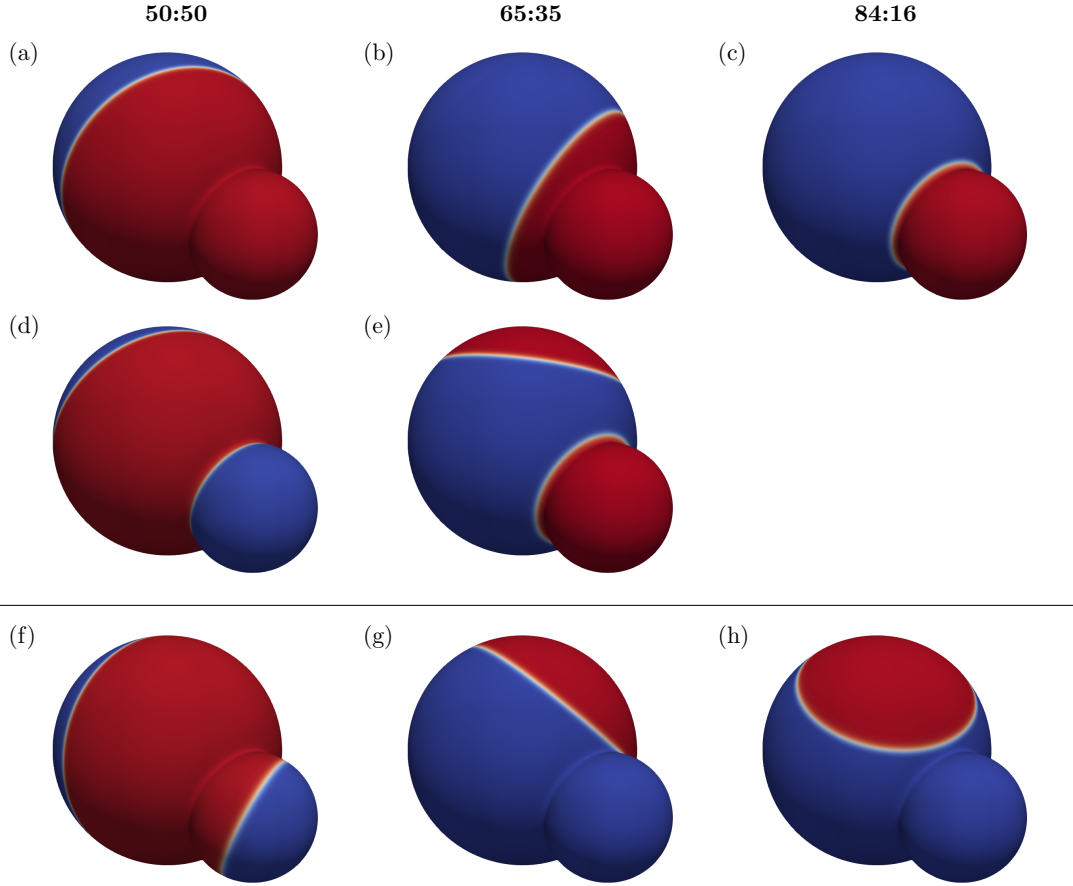


FIG. 7. Different final configurations for different compositions. (a)-(e) With bending forces. (f)-(h) Without bending forces. The configurations depend on the initial conditions.

84 : 16 is fully located in regions for positive \mathcal{H}_g , and therefore convex parts, which is a signature of isolated circular islands. These results confirm the argument in Ref. 22. We would like to remark that the strong peak for $t = 100$ and composition 50 : 50 in Fig. 6-(g) corresponds to the plateau in Fig. 6-(a) (blue curve), which results from a configuration with circular islands of equal size. The very strong increase at late times in Fig. 6-(c) corresponds to the alignment of the interface with the neck. For the composition 84 : 16 the equilibrium configuration corresponds to the occupation of the phase $\phi = -1$ on the large sphere and the phase $\phi = 1$ on the small sphere, as shown in Figs. 4 and 5.

Fig. 7 shows some different possibilities for the final configuration. They depend on the initial condition. While in the benchmark problems on a sphere in Section II E 1 any rotation of the final solution has the same energy, the considered “snowman-shape” geometry breaks this symmetry. The interface length of the final configuration depends on its position, and this dependency is most prominent for the composition 84 : 16. In Fig. 7, panels (c) and (h) show two configurations, one with bending terms and one without. The optimal solution is obtained where the interface is along the neck and it is reached for the case with bending terms, while a geodesic circle

on the large sphere is formed in the case without bending. The length of the interface l_ϵ is measured by the Cahn-Hilliard part of the energy. From the computation of the length values as in Section II E 1, we obtain $l_\epsilon = 3.1$ (with bending, Fig. 7-(c)) and $l_\epsilon = 4.6$ (without bending, Fig. 7-(h)). Thus, the bending terms favor the optimal configuration. The energy barrier between these configurations is huge as the geometry requires to enlarge the interface in order to transform the solution in Fig. 7-(h) into the one in Fig. 7-(c). Also for the other compositions, the neck plays a significant role. In Fig. 7, panels (a)-(b)-(e), the small sphere is fully covered by the phase $\phi = 1$, which is energetically favorable due to the lower bending rigidity. In Fig. 7-(d) we see the opposite: the small sphere is fully covered by the phase $\phi = -1$ and part of the interface is along the neck, and the phase $\phi = 1$ is on the energetically unfavorable large sphere. However, to further reduce the energy, either by reducing the interface or redistributing the phases, requires to move the interface away from the neck and this can only be realized by first enlarging it. So again we have an energetic barrier induced by the geometry. These configurations explain the plateaus observed in Fig. 6-(a). Without bending, we do not favor any spatial configurations. The final configurations are solely determined by minimizing the length of the interface.

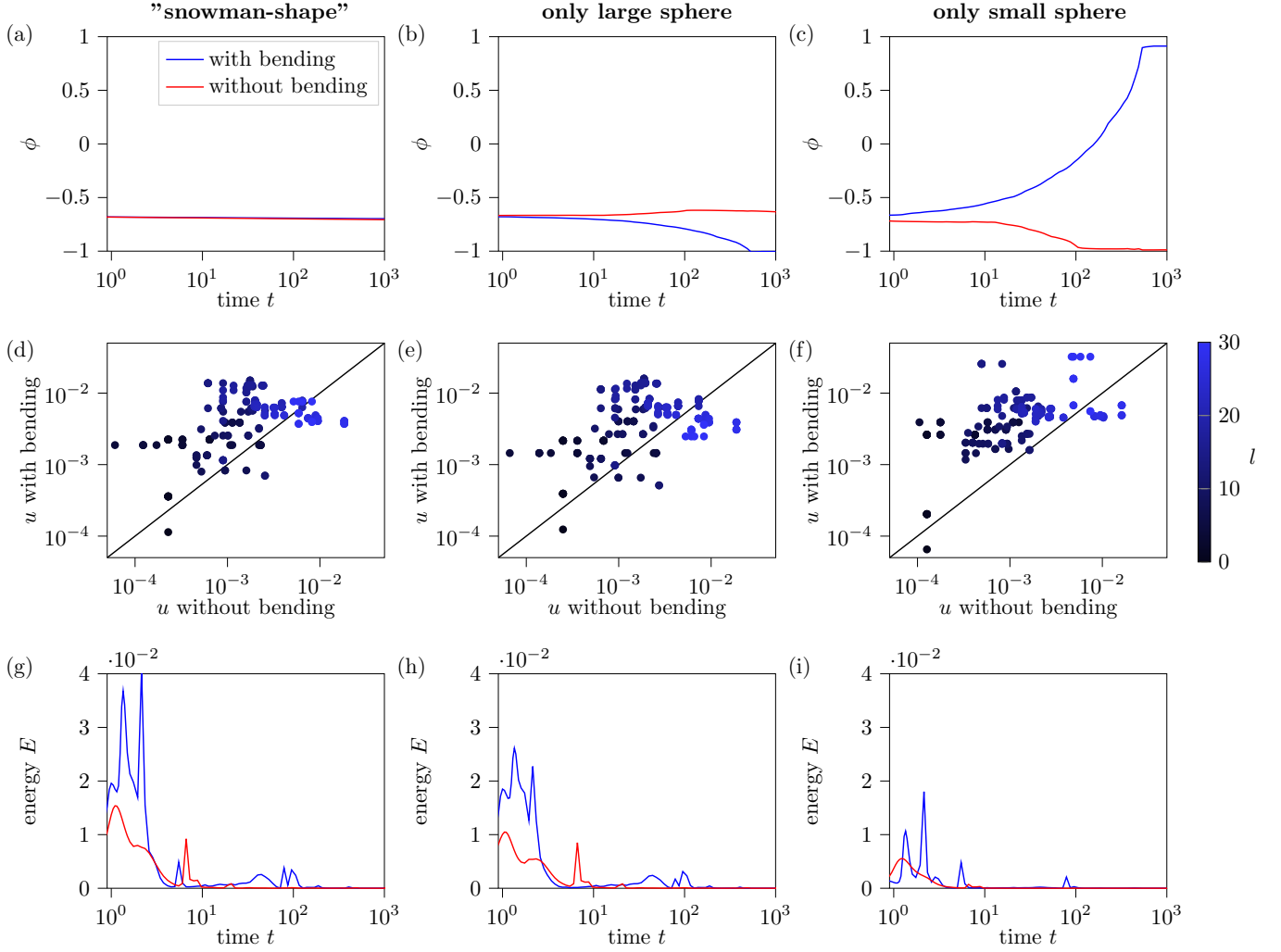


FIG. 8. Influence of the bending forces on the evolution for the distribution 84 : 16 on the “snowman-shape”. Results are shown on the whole geometry, only on the large and only on the small sphere, respectively. We compare simulations with and without bending forces. (a)-(b)-(c) Mean value of ϕ over time. (d)-(e)-(f) Comparison of the magnitude of the mean velocity u as a function of the interface length l . The values without bending terms are plotted against the corresponding values with bending terms and the interface length of the data points is color coded. (g)-(h)-(i) Evolution of the kinetic energy E with and without bending terms.

However, also this process is influenced by the geometry, as the length corresponds to the geodesic length. Computing the length of the interface l_ϵ for the corresponding compositions we have: $l_\epsilon = 6.3$ (with bending, Fig. 7-(a)), $l_\epsilon = 9.14$ (with bending, Fig. 7-(d)) and $l_\epsilon = 3.4$ (without bending, Fig. 7-(f)) for the 50 : 50 composition; $l_\epsilon = 5.5$ (with bending, Fig. 7-(b)), $l_\epsilon = 8.2$ (with bending, Fig. 7-(e)) and $l_\epsilon = 6.1$ (without bending, Fig. 7-(g)) for the 65 : 35 composition. These examples show that the bending terms can also lead to solutions that are not optimal if only the interface length is considered. This observation is in agreement with Ref. 17, where the complex interplay of composition and geometric shape has been explored for the equilibrium configurations.

We now discuss the influence of the bending terms on evolution. Not only the final spatial arrangement is influenced

by the geometric properties, but also the temporal evolution. To see this, we consider the coarsening process on the subdomains of the two different spheres of the “snowman-shape”. Fig. 8 shows simulation results for the composition 84 : 16 with $Re = 1$, with and without bending terms. Fig. 8-(a) shows the mean value of ϕ on the “snowman-shape”, which essentially just confirms the conserved evolution, and panels (b) and (c) show the mean value on the large and the small sphere, respectively. We compare the simulations with and without bending terms. With (without) bending the solution on the large sphere converges to a state with $\phi = -1$ (essentially remains at its mean value) and the solution on the small sphere converges to a state with $\phi = 1$ ($\phi = -1$). The last is due to the larger area of the large sphere, which is related to a larger probability to locate the phase $\phi = 1$ there. In Fig. 8, panels (d)-(f)

consider the influence of the bending terms on the velocity \mathbf{u} . We compute the mean velocity on the whole domain, on the large sphere, and on the small sphere at each time step. To be able to compare the results with and without bending, we consider time instances that have the same interface length l and compare these values. Fig. 8-(d)-(f) shows the comparison for the magnitude of the averaged velocities u related to the interface length l . Points above the diagonal line indicate an increased velocity due to bending forces. This is significant in all three plots but most enhanced on the small sphere. The color of the data points corresponds to the interface length l . For both situations, with and without bending terms, longer interfaces, corresponding to earlier times, are related to larger velocities. At least qualitatively, these results are confirmed by Fig. 8-(g)-(i), which show the evolution of the kinetic energy E . With bending forces, the kinetic energy is significantly larger than without bending forces, but in both situations the kinetic energy decays in time and converges to zero.

IV. DISCUSSION

We consider a detailed computational study of the role of membrane curvature on spatial arrangements of lipid phases and their evolution in idealized biomembranes. We consider multicomponent scaffolded lipid vesicles (SLV) and investigate the effect of membrane viscosity, phase-dependent bending rigidity, and phase-dependent spontaneous curvature on the coarsening process and the emerging equilibrium configurations. The mathematical model results from a phase-field approximation of a Jülicher-Lipowski energy (Ref. 24) with surface flow. It is considered on a stationary surface and can be viewed as a surface Navier-Stokes-Cahn-Hilliard model with additional phase-dependent bending terms. We solve these equations by SFEM (Refs. 50 and 51) taking into account numerical analysis results for the surface Stokes equations to ensure convergence. We carefully validate the algorithm by convergence studies of the involved subproblems. For the coupling of these subproblems, we rely on established strategies in 2D. For the physical investigations, we consider a “snowman-shape” geometry as in the experiments in Ref. 17. We identify the influence of the Reynolds number Re and the composition on the scaling behavior, consider topological and geometrical measures to explain the results, and identify the effect of the bending terms on the evolution and the reached equilibrium shape. Concerning the scaling behavior, the influence of hydrodynamics and compositions known from 2D can also be found on curved surfaces, at least qualitatively, and explained by similar arguments. However, quantitatively local geometric features, such as the considered neck in the “snowman-shape”, can lead to various local minima and extended plateaus in the coarsening process. In situations where the composition allows for a realization of the geometrically favored configuration, the hydrodynamic enhances the convergence into this configuration. In our setting, this corresponds to a composition of 84 : 16 with the phase $\phi = 1$ on the small sphere, the phase $\phi = -1$ on the large sphere, and the interface $\phi = 0$ along the neck. The phase-dependent properties in the bending rigidity and in the

spontaneous curvature influence the coarsening process. These properties guide the lipid phase with lower bending rigidity toward regions of higher mean curvature, the lipid phase with higher bending rigidity toward regions of lower mean curvature, as well as phases with spontaneous curvature toward regions with the corresponding curvature values. These bending terms are additional driving forces for the flow field and lead to the observed increase in kinetic energy.

While the considered “snowman-shape” might seem a very special case and the observed phenomena constructed, we expect these effects to have a broader impact as soon as the surface is allowed to evolve. In the evolving case, the “snowman-shape” can be related to morphologies observed in endocytosis and exocytosis. The hydrodynamically enhanced phase evolution might be a key mechanical factor in these processes. However, while endocytosis and exocytosis are addressed with phase-field models, surface viscosity is not taken into account. Numerical tools to solve the surface Navier-Stokes equations on evolving surfaces, so-called fluid deformable surfaces, have been developed (Refs. 36, 37, and 74). These approaches need to be extended to two-phase flows. However, the derivation of a corresponding thermodynamically consistent two-phase flow problem on an evolving surface requires some additional thought, see Refs. 82–85.

ACKNOWLEDGMENTS

This work was supported by the German Research Foundation (DFG) within the Research Unit “Vector- and Tensor-Valued Surface PDEs” (FOR 3013). We further acknowledge computing resources provided by ZIH at TU Dresden and by JSC at FZ Jülich, within projects WIR and PFAMDIS, respectively.

AUTHOR DECLARATIONS

Author contributions

E.B. and V.K. implemented the codes, performed all simulations, analyzed data, and contributed to conceptual development and manuscript writing. A.V. supervised the research and contributed to conceptual development, data analysis, and manuscript writing.

Competing interests

The authors declare no competing interests.

DATA AVAILABILITY

The data that support the findings of this study are available from the corresponding author upon reasonable request.

- ¹H. T. McMahon and J. L. Gallop, "Membrane curvature and mechanisms of dynamic cell membrane remodelling," *Nature* **438**, 590–596 (2005).
- ²C. A. Stanich, A. R. Honerkamp-Smith, G. G. Putzel, C. S. Warth, A. K. Lamprecht, P. Mandal, E. Mann, T.-A. D. Hua, and S. L. Keller, "Coarsening dynamics of domains in lipid membranes," *Biophys. J.* **105**, 444–454 (2013).
- ³J. Fan, T. Han, and M. Haataja, "Hydrodynamic effects on spinodal decomposition kinetics in planar lipid bilayer membranes," *J. Chem. Phys.* **133**, 235101 (2010).
- ⁴B. A. Camlay and F. L. H. Brown, "Dynamic scaling in phase separation kinetics for quasi-two-dimensional membranes," *J. Chem. Phys.* **135**, 225106 (2011).
- ⁵P. G. Saffman and M. Delbrück, "Brownian motion in biological membranes," *Proc. Natl. Acad. Sci. USA* **72**, 3111–3113 (1975).
- ⁶T. Baumgart, S. T. Hess, and W. W. Webb, "Imaging coexisting fluid domains in biomembrane models coupling curvature and line tension," *Nature* **425**, 821–824 (2003).
- ⁷T. Baumgart, S. Das, W. W. Webb, and J. T. Jenkins, "Membrane elasticity in giant vesicles with fluid phase coexistence," *Biophys. J.* **89**, 1067–1080 (2005).
- ⁸X. Wand and Q. Du, "Modelling and simulations of multi-component lipid membranes and open membranes via diffuse interface approaches," *Math. Bio.* **56**, 347–371 (2008).
- ⁹J. S. Lowengrub, A. Rätz, and A. Voigt, "Phase-field modeling of the dynamics of multicomponent vesicles: Spinodal decomposition, coarsening, budding, and fission," *Phys. Rev. E* **79**, 031926 (2009).
- ¹⁰C. M. Elliott and B. Stinner, "A surface phase field model for two-phase biological membranes," *SIAM J. Appl. Math.* **70**, 2904–2928 (2010).
- ¹¹E. L. Elson, E. Fried, J. E. Dolbow, and G. M. Genin, "Phase separation in biological membranes: Integration of theory and experiment," *Annual Review of Biophysics* **39**, 207–266 (2010).
- ¹²H. Garcke, J. Kampmann, A. Rätz, and M. Röger, "A coupled surface-Cahn-Hilliard bulk-diffusion system modeling lipid raft formation in cell membranes," *Math. Models Meth. Appl. Sci.* **26**, 1149–1189 (2016).
- ¹³P. Gera and D. Salac, "Modeling of multicomponent three-dimensional vesicles," *Computers & Fluids* **172**, 362–383 (2018).
- ¹⁴C. Zimmermann, D. Toshniwal, C. M. Landis, T. J. Hughes, K. K. Mandadapu, and R. A. Sauer, "An isogeometric finite element formulation for phase transitions on deforming surfaces," *Computer Methods in Applied Mechanics and Engineering* **351**, 441–477 (2019).
- ¹⁵P. Fonda, M. Rinaldin, D. J. Kraft, and L. Giori, "Interface geometry of binary mixtures on curved substrates," *Phys. Rev. E* **98**, 032801 (2018).
- ¹⁶P. Fonda, M. Rinaldin, D. J. Kraft, and L. Giori, "Thermodynamic equilibrium of binary mixtures on curved surfaces," *Phys. Rev. E* **100**, 032604 (2019).
- ¹⁷M. Rinaldin, P. Fonda, L. Giori, and D. J. Kraft, "Geometric pinning and antimixing in scaffolded lipid vesicles," *Nature Commun.* **11**, 4314 (2020).
- ¹⁸M. Arroyo and A. DeSimone, "Relaxation dynamics of fluid membranes," *Phys. Rev. E* **79**, 031915 (2009).
- ¹⁹I. Nitschke, A. Voigt, and J. Wensch, "A finite element approach to incompressible two-phase flow on manifolds," *J. Fluid Mech.* **708**, 418–438 (2012).
- ²⁰S. Reuther and A. Voigt, "Solving the incompressible surface Navier-Stokes equation by surface finite elements," *Phys. Fluids* **30**, 012107 (2018).
- ²¹T.-P. Fries, "Higher-order surface FEM for incompressible Navier-Stokes flows on manifolds," *Int. J. Numer. Meth. Fluids* **88**, 55–78 (2018).
- ²²V. E. Ambrus, S. Busuioc, A. J. Wagner, F. Paillusson, and H. Kusumaatmaja, "Multicomponent flow on curved surfaces: A vielbein lattice boltzmann approach," *Phys. Rev. E* **100**, 063306 (2019).
- ²³M. Olshanskii, Y. Palzhanov, and A. Quaini, "A comparison of cahn-hilliard and navier-stokes-cahn-hilliard models on manifolds," *Vietnam J. Math.* **50**, 929–945 (2022).
- ²⁴F. Jülicher and R. Lipowsky, "Domain-induced budding of vesicles," *Phys. Rev. Lett.* **70**, 2964–2967 (1993).
- ²⁵P. B. Canham, "Minimum energy of bending as a possible explanation of biconcave shape of human red blood cell," *J. Theo. Biol.* **26**, 61–76 (1970).
- ²⁶W. Helfrich, "Elastic properties of lipid bilayers - theory and possible experiments," *Zeitschrift für Naturforschung C* **28**, 693–703 (1973).
- ²⁷C. M. Elliott, L. Hatcher, and B. Stinner, "On the sharp interface limit of a phase field model for near spherical two phase biomembranes," *Interf. Free Bound.* **24**, 263–286 (2022).
- ²⁸S. Aland, S. Egerer, J. Lowengrub, and A. Voigt, "Diffuse interface models of locally inextensible vesicles in a viscous fluid," *J. Comput. Phys.* **277**, 32–47 (2014).
- ²⁹F. Haußer, W. Marth, S. Li, J. S. Lowengrub, A. Rätz, and A. Voigt, "Thermodynamically consistent models for two component vesicles," *Int. J. Biomath. Biostat.* **2**, 19–48 (2013).
- ³⁰J. S. Lowengrub, J.-J. Xu, and A. Voigt, "Surface phase separation and flow in a simple model of multicomponent drops and vesicles," *FDMP-Fluid Dyn. Mat. Proc.* **3**, 1–19 (2007).
- ³¹H. Garcke and R. Numberg, "Structure-preserving discretizations of gradient flows for axisymmetric two-phase biomembranes," *IMA J. Num. Anal.* **41**, 1899–1940 (2021).
- ³²S. Reuther and A. Voigt, "The interplay of curvature and vortices in flow on curved surfaces," *Multiscale Model. Sim.* **13**, 632–643 (2015).
- ³³I. Nitschke, S. Reuther, and A. Voigt, "Discrete exterior calculus (DEC) for the surface Navier-Stokes equation," in *Transport Processes at Fluidic Interfaces*, edited by D. Bothe and A. Reusken (Springer International Publishing, 2017) pp. 177–197.
- ³⁴S. Reuther and A. Voigt, "Erratum: 'The interplay of curvature and vortices in flow on curved surfaces'," *Multiscale Model. Sim.* **16**, 1448–1453 (2018).
- ³⁵T. Jankuhn, M. A. Olshanskii, and A. Reusken, "Incompressible fluid problems on embedded surfaces: Modeling and variational formulations," *Interf. Free Bound.* **20**, 353–377 (2018).
- ³⁶A. Torres-Sánchez, D. Millán, and M. Arroyo, "Modelling fluid deformable surfaces with an emphasis on biological interfaces," *J. Fluid Mech.* **872**, 218–271 (2019).
- ³⁷S. Reuther, I. Nitschke, and A. Voigt, "A numerical approach for fluid deformable surfaces," *J. Fluid Mech.* **900**, R8 (2020).
- ³⁸P. L. Lederer, C. Lehrenfeld, and J. Schöberl, "Divergence-free tangential finite element methods for incompressible flows on surfaces," *Int. J. Numer. Meth. Eng.* **121**, 2503–2533 (2020).
- ³⁹A. Yavari, A. Ozakin, and S. Sadik, "Nonlinear elasticity in a deforming ambient space," *J. Nonli. Sci.* **26**, 1651–1692 (2016).
- ⁴⁰H. Koba, C. Liu, and Y. Giga, "Energetic variational approaches for incompressible fluid systems on an evolving surface," *Quart. Appl. Math.* **75**, 359–389 (2017).
- ⁴¹T.-H. Miura, "On singular limit equations for incompressible fluids in moving thin domains," *Quart. Appl. Math.* **76**, 215–251 (2018).
- ⁴²H. Koba, C. Liu, and Y. Giga, "Errata to 'Energetic variational approaches for incompressible fluid systems on an evolving surface'," *Quart. Appl. Math.* **76**, 174–152 (2018).
- ⁴³J. Prüss, G. Simonett, and M. Wilke, "On the Navier-Stokes equations on surfaces," *J. Evol. Eq.* **21**, 3153–3179 (2021).
- ⁴⁴P. C. Hohenberg and B. I. Halperin, "Theory of dynamic critical phenomena," *Rev. Mod. Phys.* **49**, 435–479 (1977).
- ⁴⁵M. Gurtin, D. Polignone, and J. Vinals, "Two-phase binary fluids and immiscible fluids described by an order parameter," *Math. Modles Meth. Appl. Sci.* **6**, 815–831 (1996).
- ⁴⁶S. Aland and A. Voigt, "Benchmark computations of diffuse interface models for two-dimensional bubble dynamics," *Int. J. Numer. Meth. Fluids* **69**, 747–761 (2012).
- ⁴⁷H. Abels, H. Garcke, and G. Grün, "Thermodynamically consistent, frame indifferent diffuse interface models for incompressible two-phase flows with different densities," *Math. Modles Meth. Appl. Sci.* **22**, 1150013 (2012).
- ⁴⁸H. Abels, "On a diffuse interface model for two-phase flows of viscous, incompressible fluids with matched densities," *Arch. Rat. Mech. Anal.* **194**, 463–506 (2009).
- ⁴⁹F. Magaletti, F. Picano, M. Chinappi, L. Marino, and C. M. Casciola, "The sharp-interface limit of the Cahn-Hilliard/Navier-Stokes model for binary fluids," *J. Fluid Mech.* **714**, 95–126 (2013).
- ⁵⁰G. Dziuk and C. M. Elliott, "Finite element methods for surfaces PDEs," *Acta Num.* **22**, 289–396 (2013).
- ⁵¹M. Nestler, I. Nitschke, and A. Voigt, "A finite element approach for vector- and tensor-valued surface PDEs," *J. Comput. Phys.* **389**, 48–61 (2019).
- ⁵²O. Mickelin, J. Slomka, K. J. Burns, D. Lecoanet, G. M. Vasil, L. M. Faria, and J. Dunkel, "Anomalous chained turbulence in actively driven flows on spheres," *Phys. Rev. Lett.* **120**, 164503 (2018).
- ⁵³M. Rank and A. Voigt, "Active flows on curved surfaces," *Phys. Fluids* **33**, 072110 (2021).

- ⁵⁴R. Mendoza, J. Alkemper, and P. W. Voorhees, “The morphological evolution of dendritic microstructures during coarsening,” *Metall. Mater. Trans.* **34**, 481 (2003).
- ⁵⁵Y. Kwon, K. Thornton, and P. W. Voorhees, “Morphology and topology in coarsening of domains via non-conserved and conserved dynamics,” *Phil. Mag.* **317-335**, 90 (2010).
- ⁵⁶A. Demlow, “Higher-order finite element methods and pointwise error estimates for elliptic problems on surfaces,” *SIAM J. Num. Anal.* **47**, 805–827 (2009).
- ⁵⁷S. Praetorius and F. Stenger, “DUNE-CurvedGrid—A DUNE module for surface parametrization,” *Arch. Num. Software* **22**, 1–22 (2020).
- ⁵⁸M. Nestler, I. Nitschke, S. Praetorius, and A. Voigt, “Orientational order on surfaces: The coupling of topology, geometry, and dynamics,” *J. Nonl. Sci.* **28**, 147–191 (2018).
- ⁵⁹P. Hansbo, M. G. Larson, and K. Larsson, “Analysis of finite element methods for vector laplacians on surfaces,” *IMA J. Num. Anal.* **40**, 1652–1701 (2020).
- ⁶⁰P. Brandner, T. Jankuhn, S. Praetorius, A. Reusken, and A. Voigt, “Finite element discretization methods for velocity-pressure and stream function formulations of surface stokes equations,” *SIAM J. Sci. Comput.* **44**, A1807–A1832 (2022).
- ⁶¹M. Nestler and A. Voigt, “Active nematodynamics on curved surfaces—the influence of geometric forces on motion patterns of topological defects,” *Commun. Comput. Phys.* **31**, 947–965 (2022).
- ⁶²H. Hardering and S. Praetorius, “personal communication.”
- ⁶³T. Jankuhn and A. Reusken, “Trace finite element methods for surface vector-laplace equations,” *IMA J. Num. Anal.* **41**, 48–83 (2021).
- ⁶⁴T. Jankuhn, M. A. Olshanskii, A. Reusken, and A. Zhiliakov, “Error analysis of higher order trace finite element methods for the surface stokes equation,” *J. Num. Math.* **29**, 245–267 (2021).
- ⁶⁵H. Hardering and S. Praetorius, “Tangential errors of tensor surface finite elements,” *IMA J. Num. Anal.* (2022), 10.1093/imanum/drac015.
- ⁶⁶S. Vey and A. Voigt, “AMDIS: adaptive multidimensional simulations,” *Comput. Vis. Sci.* **10**, 57–67 (2007).
- ⁶⁷T. Witkowski, S. Ling, S. Praetorius, and A. Voigt, “Software concepts and numerical algorithms for a scalable adaptive parallel finite element method,” *Adv. Comput. Math.* **41**, 1145–1177 (2015).
- ⁶⁸A. Rätz, “A benchmark for the surface Cahn–Hilliard equation,” *Appl. Math. Lett.* **56**, 65–71 (2016).
- ⁶⁹X. Feng and A. Prohl, “Numerical analysis of the Allen–Cahn equation and approximation for mean curvature flows,” *Num. Math.* **94**, 33–65 (2003).
- ⁷⁰A. Jokisaari, P. Voorhees, J. Guyer, J. Warren, and O. Heinonen, “Benchmark problems for numerical implementations of phase field models,” *Comput. Mater. Sci.* **126**, 139–151 (2017).
- ⁷¹A. Rätz and A. Voigt, “PDE’s on surfaces - a diffuse interface approach,” *Commun. Math. Sci.* **4**, 575–590 (2006).
- ⁷²T. Witkowski, R. Backofen, and A. Voigt, “The influence of membrane bound proteins on phase separation and coarsening in cell membranes,” *Phys. Chem. Chem. Phys.* **14**, 14509–14515 (2012).
- ⁷³B. Gross and P. J. Atzberger, “Hydrodynamic flows on curved surfaces: Spectral numerical methods for radial manifold shapes,” *J. Comput. Phys.* **371**, 663–689 (2018).
- ⁷⁴V. Krause and A. Voigt, “A numerical approach for fluid deformable surfaces with conserved enclosed volume,” *arXiv* (2022), 10.48550/ARXIV.2210.03585.
- ⁷⁵We note a typing error in Ref. 33 which has been confirmed by the authors.
- ⁷⁶A. Wagner and J. Yeomany, “Breakdown of scale invariance in the coarsening of phase-separating binary fluids,” *Phys. Rev. Lett.* **80**, 1429 (1998).
- ⁷⁷Y. Wang, Y. Palzhanov, A. Quaini, M. Olshanskii, and S. Majd, “Lipid domain coarsening and fluidity in multicomponent lipid vesicles: A continuum based model and its experimental validation,” *Biochimica et Biophysica Acta (BBA)-Biomembranes* **1864**, 183898 (2022).
- ⁷⁸H. Henry and G. Tegze, “Kinetics of coarsening have dramatic effects on the microstructure: Self-similarity breakdown induced by viscosity contrast,” *Phys. Rev. E* **100**, 013116 (2019).
- ⁷⁹W. B. Andrews, K. L. M. Elder, P. W. Voorhees, and K. Thornton, “Effect of transport mechanism on the coarsening of bicontinuous structures: A comparison between bulk and surface diffusion,” *Phys. Rev. Mat.* **4**, 013401 (2020).
- ⁸⁰P. C. Fife and O. Penrose, “Interfacial dynamics for thermodynamically consistent phasefield models with nonconserved order parameter,” *Electr. J. Diff. Eq.* **16**, 1–49 (1995).
- ⁸¹M. Benes, M. Kolar, J. M. Sischka, and A. Voigt, “Degenerate area preserving surface allen-cahn equation and its sharp interface limit,” *arXiv* (2023).
- ⁸²S. C. Al-Izzi and R. G. Morris, “Active flows and deformable surfaces in development,” *Seminars in Cell & Developmental Biology* **120**, 44–52 (2021).
- ⁸³L. A. Hoffmann, L. N. Carenza, J. Eckert, and L. Giomi, “Theory of defect-mediated morphogenesis,” *Sci. Adv.* **8**, eabk2712 (2022).
- ⁸⁴I. Nitschke and A. Voigt, “Observer-invariant time derivatives on moving surfaces,” *J. Geom. Phys.* **173**, 104428 (2022).
- ⁸⁵I. Nitschke, S. Sadik, and A. Voigt, “Tangential tensor fields on deformable surfaces – how to derive consistent L^2 -gradient flows,” *arXiv* (2022), 10.48550/arXiv.2209.13272.